



## On the efficacy of Xe<sup>+</sup>-pFIB preparation to avoid Ga<sup>+</sup>-FIB induced phase transformations in Al-Ni alloys

Hendrik C. Jansen<sup>a,b,\*</sup>, Amit Sharma<sup>a,c</sup>, Krzysztof Wiecezrak<sup>a,d</sup>, Ganesh K. Nayak<sup>e</sup>,  
Jochen M. Schneider<sup>e</sup>, Jakob Schwiedrzik<sup>a,f</sup>, Thomas E.J. Edwards<sup>a,g,\*</sup>, Johann Michler<sup>a,b</sup>

<sup>a</sup> Laboratory for Mechanics of Materials and Nanostructures, Empa Swiss Federal Laboratories for Material Science and Technology, Feuerwerkerstrasse 39, CH-3602 Thun, Switzerland

<sup>b</sup> École Polytechnique Fédérale de Lausanne, Rte Cantonale, CH-1015 Lausanne, Switzerland

<sup>c</sup> SwissCluster AG, Bahnhofstrasse 19, CH-3700 Spiez, Switzerland

<sup>d</sup> Department of Materials Science, Faculty of Mechanical Engineering and Aeronautics, Rzeszow University of Technology, al. Powstancow Warszawy 12, 35-959 Rzeszow, Poland

<sup>e</sup> Materials Chemistry, RWTH Aachen University, Kopernikusstrasse 10, D-52074 Aachen, Germany

<sup>f</sup> Laboratory for High Performance Ceramics, Empa Swiss Federal Laboratories for Material Science and Technology, Überlandstrasse 129, CH-8600 Dübendorf, Switzerland

<sup>g</sup> Research Center for Structural Materials, National Institute for Materials Science, 1-2-1 Sengen, Tsukuba 305-0047, Japan

### ARTICLE INFO

#### Keywords:

Nanocrystalline aluminium  
Intermetallic phases  
Phase transformation  
Gallium  
Focused Ion Beam (FIB) sample preparation

### ABSTRACT

Preparation of an Al-Ni alloy for transmission electron microscopy (TEM) by focused ion beam (FIB) milling using Ga<sup>+</sup> ions induced phase transformations, risking misinterpretation: from FCC Al-Ni solid solution to FCC Al-Ni and orthorhombic Al<sub>3</sub>Ni phases. Upon milling a nanolaminated Al<sub>95</sub>Ni<sub>5</sub>-AlO<sub>x</sub> thin film with Ga<sup>+</sup> ions, local Ga segregations of up to 15 at.% and the concurrent formation of orthorhombic regions are observed. This is consistent with density functional theory calculations indicating that the orthorhombic structures with and without Ga are more stable than the corresponding FCC compositions probed here. In contrast, Xe<sup>+</sup> plasma FIB preparation did not alter the microstructure and the maximum Xe-content reached only 0.2 at.%. TEM-analysis did not reveal significant strain differences of the Al-Ni solid solution and Al<sub>3</sub>Ni. Hence, we recommend the use of Xe<sup>+</sup>-pFIB for sample preparation of alloys which are sensitive to Ga-induced phase transformations such as Al<sub>95</sub>Ni<sub>5</sub> to prevent misinterpretation.

Both micromechanical testing and high spatial resolution analysis of materials require the preparation of geometrically-tailored specimens. Focused Ion Beam (FIB) microscopes of various kinds were introduced as sample preparation methods for such nanoscale structures. Options arise among highly localised sputtering from ion bombardment with either Ga in conventional FIB [1–4]; or Xe, Ne, He, O, and N-based plasma FIB (pFIB) systems and cryo-(p) FIB to avoid Ga contamination [5,6] and to slow down Ga diffusion [7], respectively.

Researchers have repeatedly shown that Ga<sup>+</sup>-FIB preparation of stainless steel triggers phase transformation from an austenitic parent lattice towards ferrite [6,8–11]. In fact, Knippling *et al.* [8] first linked the FIB-induced transformation in austenitic 316L steels to the austenite stability influenced by ion dose and crystallographic orientation. Transformation was observed at FIB parameters of 30 kV and 100 pA at ion doses of roughly 10<sup>15</sup> ions cm<sup>-2</sup> [8], in the case of 304 stainless steel,

even with Xe<sup>+</sup> ions [6], due to a coupled chemical and atomic rearrangement upon bombardment with keV energy ions [9–11]. Chemically, duplex stainless steel was reported to transform due to Ga-induced ferrite stabilisation, while the austenite grain orientation determined ion channelling – stronger transformation tendencies were linked to lesser ion channelling [11]. On the other hand, phase transformation was derived from collision-triggered atomic rearrangement, i.e. defect formation in the form of increasing dislocation density, especially in austenite grains of crystal orientations less conducive to ion channelling. Stopping and Range of Ions in Matter (SRIM) simulations [12] correctly predicted the shorter transformation depth where ions actively change the microstructure of Xe<sup>+</sup> compared to Ga<sup>+</sup> ions, due to a lesser sample strain by reduced Xe implantation and hence a lower far field stress effect [9].

Upon interaction of high energy ions with Aluminium, Ga<sup>+</sup>

\* Corresponding authors.

E-mail addresses: [hendrik.jansen@empa.ch](mailto:hendrik.jansen@empa.ch) (H.C. Jansen), [thomas.edwards@nims.go.jp](mailto:thomas.edwards@nims.go.jp) (T.E.J. Edwards).

<https://doi.org/10.1016/j.scriptamat.2025.116589>

Received 11 November 2024; Received in revised form 27 January 2025; Accepted 29 January 2025

Available online 9 February 2025

1359-6462/© 2025 The Authors. Published by Elsevier Inc. on behalf of Acta Materialia Inc. This is an open access article under the CC BY license (<http://creativecommons.org/licenses/by/4.0/>).

bombardment has been reported to induce an amorphous Ga-rich surface layer and atomic Ga segregation along the grain boundaries [4, 13–18]. Ga<sup>+</sup>-irradiation during FIB microscopy causes Ga-induced liquid metal embrittlement (LME), grain boundary dewetting and crack formation [19], as well as formation of a low-melting Al-Ga eutectic [20]. Yet, there are only a few studies that actively discuss the in-volume modification of Al through Ga. 30 kV Ga<sup>+</sup>-FIB preparation was reported to induce strong segregation of Ga at incoherent Al<sub>3</sub>Mg<sub>2</sub> particles occupying the grain boundaries in AA 5083 Al alloy [13]. Ruan *et al.* [15] highlighted the implantation of Ga in nanocrystalline Al-Mn during Ga<sup>+</sup>-FIB sample preparation following the Thompson needle preparation method [21]. Atom probe tomography (APT) revealed Ga segregation with highly localised content up to 3 at.% in the Mn-rich transformed amorphous Al-Mn region. Moreover, Gault *et al.* [4] reported high-density dislocation regions and high-angle grain boundaries in Al<sub>3</sub>(Sc,Zr) and Al-Mg-Zn-Cu, respectively, as more likely to be decorated by Ga. Ga<sup>+</sup>-FIB prepared polycrystalline Al micropillars, even polished with low 2-5 kV, showed reduced mechanical properties compared to Xe<sup>+</sup>-pFIB micropillar fabrication [22,23].

Fortunately, in recent years, alternative preparation by cryo-Ga<sup>+</sup>-FIB and Xe<sup>+</sup>-pFIB showed prevented Ga decoration of interfaces in Al [4,5,7, 17,23]. Liliensten and Gault [7] applied cryo- Ga<sup>+</sup>-FIB preparation of 6016 aluminium and APT to show significant reduction of Ga at an Al grain boundary by more than 15 at.% to roughly 0.25 – 0.5 at.%. Indeed, cryo- Ga<sup>+</sup>-FIB preparation at ca. 82 K reduced the diffusion coefficient of Ga in Al by roughly ten orders of magnitude and hence enables substantially reduced Ga-decoration at the Al Grain Boundary [7,20,24].

Xe<sup>+</sup>-pFIB preparation of polycrystalline Al is reported to not generate Xe enrichments at interfaces such as grain boundaries, and additionally induces comparable lattice distortions in the crystal lattice as conventional Ga<sup>+</sup>-FIB, based on SRIM calculations [4,5].

Here we advance evidence that conventional Ga<sup>+</sup>-FIB TEM sample preparation of nanocrystalline Al alloys is even able to induce phase transformation similarly to the austenitic stainless steel case [6,8–11]. Upon Ga<sup>+</sup>-FIB preparation of nanolaminated Al<sub>95</sub>Ni<sub>5</sub> – AlO<sub>x</sub> thin films (bilayers: 25 – 1 nm thick; total film thickness 3 μm; see Fig. 1a), an unexpected heterogeneous microstructure was observed. The detailed purpose and investigation of this nanolaminated Al<sub>95</sub>Ni<sub>5</sub> – AlO<sub>x</sub> thin film will be the subject of a later work. To the current purpose, room temperature TEM samples were prepared by both Ga<sup>+</sup>-FIB as well as Xe<sup>+</sup>-pFIB, and their crystallography and chemistry were subsequently analysed by (scanning)TEM (S/TEM). The thin films were deposited by means of combined hybrid physical vapour (PVD) and atomic layer deposition (ALD) in a SwissCluster AG SC-1 cluster deposition chamber, similarly to several previous publications by the co-authors [25–28]. Conventional “lift-out” procedures [2,29] were applied to prepare site-specific TEM specimens. FIB parameters applied for the preparation of the specimens can be found in Table 1. Samples were prepared using a TESCAN LYRA3 FIB-SEM in the case of Ga<sup>+</sup>-FIB and a ThermoFisher Scientific Helios 5 Hydra DualBeam pFIB-SEM equipped for Xe<sup>+</sup> milling. Finally, TEM was conducted on a ThermoFisher aberration corrected (probe) Themis 200 G3 operated at 200 kV. Analysis of S/TEM images and selected area electron diffraction (SAED) patterns was conducted using the CrystBox software [30].

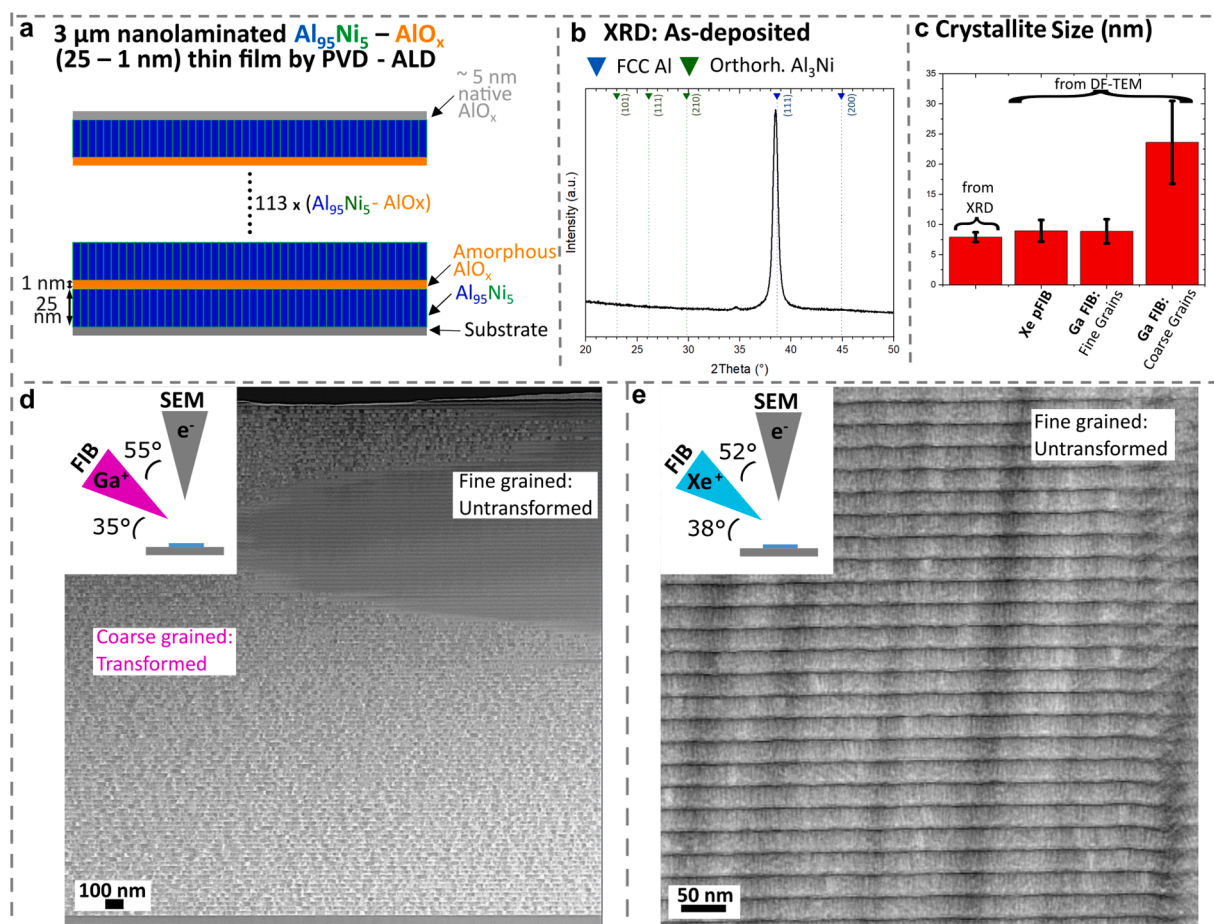


**Fig. 1.** Overall scope of the current investigation: (a) targeted Al<sub>95</sub>Ni<sub>5</sub> – AlO<sub>x</sub> (25 – 1 nm) thin film architecture, (b) Bragg-Brentano XRD of as-deposited Al<sub>95</sub>Ni<sub>5</sub> – AlO<sub>x</sub> sample, (c) lateral FCC Al grain size derived from XRD in (b) as well as from Dark Field TEM by Ga<sup>+</sup> and Xe<sup>+</sup>-FIB prepared samples, (d) FIB arrangement and representative HAADF-STEM image from Ga<sup>+</sup>-FIB indicating the phase transformation, and (e) FIB arrangement and representative HAADF-STEM image from Xe<sup>+</sup>-pFIB.

**Table 1**  
Applied FIB parameters for TEM-specimen preparation.

FIB System	Trenching (kV / nA)	Thinning (kV / nA / ° Overtilt)	Polishing (kV / nA / ° Overtilt)	Total Ion Dose (derived from [31]) (ions $\times$ cm <sup>-2</sup> )
Ga <sup>+</sup> -FIB	30 / 10	30 / 1 – 0.03 / 1 – 1.5	5 / 0.03 / 5	$\sim 6.0 \times 10^{19}$
Xe <sup>+</sup> -pFIB	30 / 65	30 / 1 – 0.1 / 1 – 2	5 / 0.03 / 5	$\sim 7.7 \times 10^{19}$

The diffractogram in Fig. 1b confirms the dominant (111) FCC Al texture of the Al<sub>95</sub>Ni<sub>5</sub> – AlO<sub>x</sub> thin film, corresponding to the crystalline Al<sub>95</sub>Ni<sub>5</sub> solid solution, while the AlO<sub>x</sub> interlayers are reported to be X-ray amorphous. The peak at  $2\theta = 34.8^\circ$  stems from the Cu K  $\beta$  (111) FCC Al. The out-of-plane grain size was controlled to be 25 nm from the deposition rate; the lateral grain sizes measured by different routes are depicted in Fig. 1c. A FCC Al crystallite size of roughly  $7.9 \pm 0.8$  nm was derived from the Bragg Brentano X-ray Diffraction (XRD) applying the Scherrer equation with Shape Factor equal to 1, corrected by a LaB<sub>6</sub> standard at  $2\theta = 40^\circ$ . The High Angle Annular Dark Field (HAADF) STEM imaging from a Ga<sup>+</sup>-FIB prepared TEM specimen in Fig. 1d emphasizes the heterogeneity resulting from this preparation routine, showing both a fine- and a coarse-grained region of  $8.9 \pm 2$  nm and  $23.6 \pm 6.9$  nm, respectively. In contrast, the HAADF-STEM overview image of a Xe<sup>+</sup>-pFIB prepared TEM specimen, Fig. 1e, confirms the imprint of a homogenous microstructure with as-mentioned lateral grain size of  $8.95 \pm 1.8$  nm, being in good agreement with the results from XRD and DF-TEM of the fine-grained region when prepared with a Ga<sup>+</sup>-FIB.

The in-depth S/TEM analysis of the Ga<sup>+</sup>-FIB and Xe<sup>+</sup>-pFIB preparation of TEM specimens is displayed in Fig. 2. The HAADF-STEM images in Fig. 2a shows a representative region of the Ga<sup>+</sup>-FIB prepared Al<sub>95</sub>Ni<sub>5</sub> – AlO<sub>x</sub> thin film: two different microstructures are evident. The SAED patterns in Fig. 2b confirms FCC Al in one region, whereas SAED of the altering microstructure in Fig. 2d displays more features. In fact, the d-spacings of 0.216 nm and 0.133 nm do not correspond to FCC Al, but rather match the {112} and {242} planes of orthorhombic Al<sub>3</sub>Ni [30, 32]. Additionally, Fast Fourier Transformation (FFT) of HR-STEM images of the coarse-grained transformed region confirms the presence of both FCC Al and orthorhombic Al<sub>3</sub>Ni as illustrated in Fig. 2c and e,

respectively.

The Energy Dispersive X-ray Spectroscopy (EDS) maps of the Ga<sup>+</sup> FIB-prepared thin film cover both coarse-grained and fine-grained microstructures, as visualised in Fig. 2f-h. Beyond the well-reported segregation of Ga at Al interfaces [4,13–18], Fig. 2g confirms the preferential Ga decoration of the coarse-grained region and nearby AlO<sub>x</sub> interlayers. In fact, the fine-grained FCC Al microstructure shows a homogenous distribution of roughly 1.3 at.% Ga in the Al matrix and Al-Al grain boundaries. However, confident determination of grain boundary segregation is impeded by the grain size versus specimen thickness yield. The nearby amorphous AlO<sub>x</sub> interlayers apparently contain approximately 1.3at.% of Ga, although again this analysis is complicated by considering the 1 nm thickness with respect to 50 – 80 nm lamella thickness. In contrast, the coarse-grained region with both FCC Al and orthorhombic Al<sub>3</sub>Ni grains exhibits a more heterogeneous Ga distribution. While the coarse Al and Al<sub>3</sub>Ni grains incorporate already more Ga > 5 at.%, the Ga decoration of the Al-Al<sub>3</sub>Ni and Al<sub>3</sub>Ni-Al<sub>3</sub>Ni grain boundaries reaches up to 12 and 15 at.%, respectively. Therefore, Ga can be found preferentially in the proximity of the Al<sub>3</sub>Ni grains. Considering the stable AlO<sub>x</sub> layer thickness, no clear change in chemistry or crystallography of the AlO<sub>x</sub> through Ga incorporation can be concluded. For visualisation of corresponding STEM-EDS maps including the Al- and O-mapping, the reader is referred to the supplementary material (Suppl. 1). In good agreement with the crystallographic analysis, Fig. 2c and e clearly link the presence of both Al and Al<sub>3</sub>Ni phases to local Ni and Ga agglomeration. The Ni-content according to STEM-EDS reaches up to 15 at.% in regions containing Al<sub>3</sub>Ni grains identified by diffraction, whereas the coarse FCC Al grains become Ni-deficient with only 1.5 at.% of Ni.

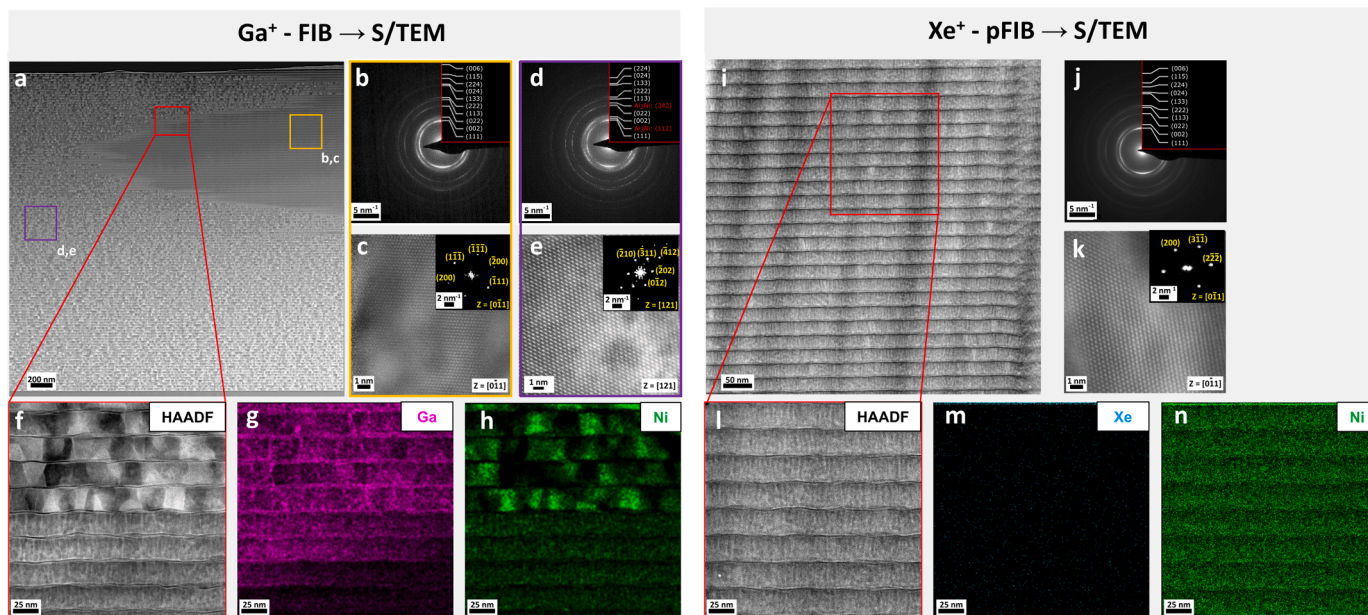


**Fig. 2.** (a – h) S/TEM investigation of Ga<sup>+</sup>-FIB prepared specimen: (a) HAADF-STEM overview image, fine grain region (b) SAED pattern and (c) HR-STEM image with FFT pattern, coarse grain (d) SAED pattern and (e) HR-STEM image with FFT pattern, as well as (f) magnified HAADF-STEM image with corresponding (g) Ga EDS map, and (h) Ni EDS map. (i – n) S/TEM investigation of Xe<sup>+</sup>-pFIB prepared specimen: (i) HAADF-STEM overview image, (j) SAED pattern, (k) HR-STEM image with FFT pattern, as well as (l) zoomed-in HAADF-STEM image with corresponding (m) Xe EDS map and (n) Ni EDS map.

In contrast, Fig. 2i - n shows representative S/TEM images of a nearby region of the same thin film when the TEM specimen was prepared by  $\text{Xe}^+$ -pFIB. The HAADF-STEM image illustrated in Fig. 2i shows only a single microstructure type: similar to the fine-grained region of the  $\text{Ga}^+$ -FIB prepared specimen. Namely, a homogenous lateral and out-of-plane Al grain size of  $8.9 \pm 2$  nm and 25 nm, respectively, as well as intact 1 nm amorphous  $\text{AlO}_x$ . Additionally, both the SAED and FFT images in Fig. 2j and Fig. 2k confirm the crystal structure to be solely FCC Al. Hence, the  $\text{Ga}^+$ - and  $\text{Xe}^+$ -FIB prepared  $\text{Al}_{95}\text{Ni}_5 - \text{AlO}_x$  show distinct microstructure and crystallography. XRD indicates that FCC Al is the sole crystalline phase present in the as-deposited state. Fig. 2m confirms homogenous but marginal Xe-contents of roughly 0.2 at.% in  $\text{Al}_{95}\text{Ni}_5 - \text{AlO}_x$  by STEM-EDS after  $\text{Xe}^+$ -pFIB preparation – negligible within the accuracy of STEM-EDS [33]. Additionally, the Ni-profile of the corresponding sample in Fig. 2n shows homogenous Ni-distribution of ca. 5 at.%, agreeing with the fine-grained FCC Al in Fig. 2h in the case of  $\text{Ga}^+$ -FIB. Hence, the fine-grained microstructure can be linked to a  $\text{Al}_{90}\text{Ni}_5$  solid solution incorporating roughly 5 at.% of oxygen (supplementary material). We therefore conclude that  $\text{Ga}^+$ -irradiation of metastable Al-Ni during conventional FIB milling procedures triggers a phase transformation from FCC Al to orthorhombic  $\text{Al}_3\text{Ni}$ , along with coarsening of the remaining FCC phase: this can be avoided by  $\text{Xe}^+$ -pFIB preparation.

Based on the observations, either bombardment kinetics or chemical stabilisation through ion implantation can be analysed as a transformation trigger as in previous stainless steel studies [6,9,10]. The SAED of both  $\text{Ga}^+$  and  $\text{Xe}^+$ -FIB prepared  $\text{Al}_{95}\text{Ni}_5 - \text{AlO}_x$  thin films indicate that ion bombardment does not give rise to a noticeable atomic rearrangement (e.g. Frenkel defects) of the FCC Al lattice. In fact, the calculated spacings of respective  $\{111\}$ ,  $\{002\}$ ,  $\{022\}$ , and  $\{113\}$  FCC Al planes do not deviate between  $\text{Ga}^+$  and  $\text{Xe}^+$ -FIB prepared AlNi –  $\text{AlO}_x$  thin films with 0.232 nm, 0.201 nm, 0.142 nm, and 0.121 nm, respectively. Rather, these match (within 0.17%) calculated lattice plane spacings of the FCC  $\text{Al}_{95}\text{Ni}_5$  solid solution derived from Vegard's law with lattice parameters of 0.404 nm and 0.348 nm for FCC Al and FCC Ni, respectively. XRD from Fig. 1 confirms the  $\{111\}$  FCC Al to possess a lattice spacing of roughly 0.234 nm, showing 0.86% deviation from TEM-derived 0.232 nm. Additionally, SAED analysis of the  $\{112\}$  and  $\{242\}$  peaks of  $\text{Al}_3\text{Ni}$  grains also indicate no significant atomic rearrangement. FFT analysis of the HR-STEM images from the two  $\text{Ga}^+$ -FIB fine- and coarse-grained FCC Al, as well as the  $\text{Xe}^+$ -pFIB FCC Al, similarly do not show atomic rearrangement differences between the two preparation routes. The  $\{111\}$  and  $\{200\}$  FCC Al planes in every case show less than 1% deviation between (un-)transformed regions. It is worthwhile mentioning that Shimizu *et al.* [10] linked conventional TEM-derived 1% strain (of atomic rearrangement), and the related hydrostatic stress field from  $> 10$  at.% Ga in the lattice, to causing phase transformation in austenitic steel. However, strain calculation based on conventional S/TEM usually only allows strain determination with an accuracy of  $> 2\%$  strain [34], whereas high angular resolution Transmission Kikuchi Diffraction (TKD) allows accuracies of up to  $< 0.2\%$  strain [34–36]. Here, the effective use of TKD is prevented by the ultra-fine grain size here of only 10 nm. Zhong *et al.* [5] justified phase transformation in Al by ion bombardment-induced atomic rearrangement through 30 kV  $\text{Ga}^+$  and 30 kV  $\text{Xe}^+$ . SRIM calculations determined the average energy transfer to Al to be 4.48 keV/ion and 4.79 keV/ion at  $89^\circ$  incidence, for 30 kV  $\text{Ga}^+$  and 30 kV  $\text{Xe}^+$  respectively [5]. Thus, both irradiation by 30 kV  $\text{Ga}^+$  and 30 kV  $\text{Xe}^+$  should trigger transformation equivalently. However, there is no phase transformation visible in the case of  $\text{Xe}^+$ -pFIB prepared  $\text{Al}_{95}\text{Ni}_5 - \text{AlO}_x$ , but only through  $\text{Ga}^+$ -FIB preparation. Hence, both the theoretical SRIM modelling from the work of Zhong *et al.* [5] and S/TEM-imaging refute atomic arrangement differences between  $\text{Ga}^+$  and  $\text{Xe}^+$  in Al, but the phase transformation here only occurs due to  $\text{Ga}^+$ , and not  $\text{Xe}^+$ , irradiation. These results give a first hint that the phase transformation of nanocrystalline FCC Al to coarser-grained FCC Al and orthorhombic  $\text{Al}_3\text{Ni}$  is due to Ga acting as an

$\text{Al}_3\text{Ni}$  stabiliser.

Hence, the alternative trigger for phase transformation could be a thermodynamically stabilised microstructure through either Ga or Xe implantation [9,11,37]. We focus on the crystalline Al-Ni layers due to the fact that the amorphous  $\text{AlO}_x$  does not show phase transformation despite Ga agglomeration around the interface. It is worthwhile mentioning that the FIB “lift-out” and “thinning” process with  $\text{Ga}^+$  and  $\text{Xe}^+$  induce lamella-adjacent ion doses of roughly  $6 \times 10^{19}$  and  $7.7 \times 10^{19}$  ions  $\text{cm}^{-2}$ , respectively. These values were derived from the bombarded area at respective current visible in Table 1 during milling and polishing. In this case, 10 nA trenching in case of  $\text{Ga}^+$ -FIB induces lamella-adjacent  $\text{Ga}^+$  doses of roughly  $9 \times 10^{18}$  ions  $\text{cm}^{-2}$  when milling a  $20 \times 20 \mu\text{m}^2$  rectangle at a depth of roughly 15  $\mu\text{m}$  for in total 600 s for both sides. Ion doses per preparation step can be found in the Supplementary Material. Here, the calculated  $\text{Xe}^+$  dose is slightly higher (28%), which might have larger atomic rearrangement, but only Ga triggers phase transformation.  $\text{Ga}^+$ -bombardment of a previously  $\text{Xe}^+$ -pFIB prepared TEM lamella was carried out here to determine the critical preparation step. The findings are displayed in the Supplementary Material: it confirms that 30 kV  $\text{Ga}^+$ -bombarding according to the “thinning” procedure did not trigger any Ni diffusion or Ga incorporation despite Ga doses of up to  $9 \times 10^{17}$  ions  $\text{cm}^{-2}$ .

Density Functional Theory (DFT) calculations were carried out to determine the formation enthalpy of both orthorhombic and FCC  $\text{Al}_3\text{Ni}$  models. Calculations covered a supercell of  $\text{Al}_{48}\text{Ni}_{16}$ , a FCC Al reference cell, as well as  $\sim 5$  at.% Ga-containing supercells  $\text{Al}_{45}\text{Ni}_{16}\text{Ga}_3$ ,  $\text{Al}_{46}\text{Ni}_{15}\text{Ga}_3$ ,  $\text{Al}_{47}\text{Ni}_{14}\text{Ga}_3$ , and  $\text{Al}_{48}\text{Ni}_{13}\text{Ga}_3$  compounds. DFT simulations were performed with the Vienna Ab Initio Simulation Package (VASP) [38,39]. The various compositions were chosen to represent STEM-EDS measured Ga concentration levels for Al or Ni sublattice atoms. The distribution of the Ga atoms, while replacing Al or/and Ni, were achieved by the special quasi-random structure (SQS) method [40] to simulate random mixing. Fig. 3 suggests that all calculated compounds, despite FCC Al-Ni, are thermodynamically stable, with orthorhombic  $\text{Al}_3\text{Ni}$  ( $\triangleq \text{Al}_{48}\text{Ni}_{16}$ ) the most stable. It is evident that Ga incorporation in either Al or Ni sublattices leads to the formation of metastable phases, stabilizing the orthorhombic phases more than the FCC phases. The most stable configuration among the metastable phases was achieved when replacing Ga on the Al sublattice in the case of orthorhombic  $\text{Al}_{45}\text{Ni}_{16}\text{Ga}_3$ . The marginal energetic penalty of 13 meV in the case of orthorhombic  $\text{Al}_{45}\text{Ni}_{16}\text{Ga}_3$  when replacing Ga onto Al

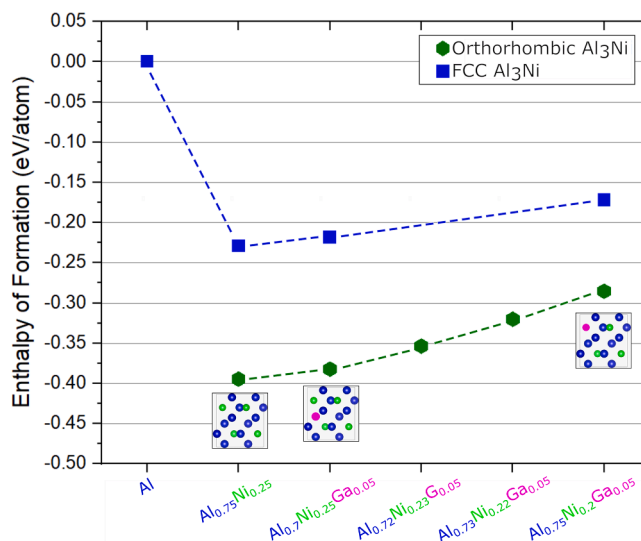


Fig. 3. Enthalpy of formation of FCC and orthorhombic  $\text{Al}_3\text{Ni}$  (modeled with  $\text{Al}_{48}\text{Ni}_{16}$  supercell) and  $\sim 5$  at.% Ga-containing compounds modeled with supercell  $\text{Al}_{45}\text{Ni}_{16}\text{Ga}_3$ ,  $\text{Al}_{46}\text{Ni}_{15}\text{Ga}_3$ ,  $\text{Al}_{47}\text{Ni}_{14}\text{Ga}_3$ , and  $\text{Al}_{48}\text{Ni}_{13}\text{Ga}_3$  calculated by density functional theory, insets showing representative 16 atoms cell.

sublattice atom sites poses a weak thermodynamic barrier to the formation of metastable Ga-containing Al-Ni compounds. Regarding the thermodynamics of orthorhombic Al<sub>3</sub>Ni formation, Michaelsen *et al.* [41] derived the activation energy of formation of orthorhombic Al<sub>3</sub>Ni to be 1.5 eV, whereas formation was not observed at  $T < 500$  K [42]. Larsen *et al.* [43] showed that Al<sub>3</sub>Ni is kinetically impeded to form from elemental multilayered Al/Ni films even under incident 500 keV Xe<sup>+</sup> irradiation due to a limited amount of collision cascades. Only ion irradiation at  $T > 400$  K allowed exceeding the kinetic barrier to form crystalline Al<sub>3</sub>Ni when the Ni-content of Al-Ni is below 30 at.%. Building on the work of Meingailis [44] and Ishitani and Kaga [45], we calculated that Ga<sup>+</sup> bombardment (10 nA, 30 kV) on Al-based materials, with a ~125 nm beam spot and ~6.5 A cm<sup>-2</sup> current density, could cause a local temperature rise of approximately 50 K. Using the diffusion data from Peterson and Rothman [24], the bulk diffusion coefficient of Ga in Al-based materials at 323 K is estimated to be  $8.23 \times 10^{-25}$  m<sup>2</sup> s<sup>-1</sup>, while the grain boundary diffusion coefficient is about 13 orders of magnitude higher [20]. Consequently, micron-scale Ga diffusion laterally and in-depth is anticipated, consistent with the diffusion behavior observed during conventional Ga<sup>+</sup>-FIB lamella preparation of Al at room temperature, where diffusion coefficients of  $5.57 \times 10^{-27}$  m<sup>2</sup> s<sup>-1</sup> [7] and  $5.83 \times 10^{-9}$  m<sup>2</sup> s<sup>-1</sup> [20] are reported for bulk and grain boundary, respectively. Ultimately, transformation of the metastable Al<sub>95</sub>Ni<sub>5</sub> solid solution towards a Ga-containing orthorhombic Al<sub>3</sub>Ni phase could be triggered through a combined thermodynamic and kinetic effort through keV energy excitation with subsequent lattice vibrations and the chemical effect of Ga stabilizing the orthorhombic Al<sub>3</sub>Ni, respectively.

A recent study of Jimenez *et al.* [46] of nanolaminated elemental Al-Ni thin films did not show any phase transformation with either Ga<sup>+</sup>-FIB or Xe<sup>+</sup>-pFIB preparation. While the authors claim that Ga<sup>+</sup>-FIB preparation “could” lead to the presence of Ga-containing Al-Ni intermetallics at the Al-Ni interface, the findings here clearly prove the modification of an Al-Ni solid solution through Ga incorporation.

Hence, employing Ga<sup>+</sup>-FIB as a preparation method for high spatial resolution microscopy of multi-element Al-alloys might introduce artefacts beyond surface and interface decoration.

Lilensten and Gault [7] proposed cryo-Ga<sup>+</sup>-FIB as a go-to technique for preparation of Al samples for high-resolution microscopy without interface decoration of Ga. APT-reported 0.25 – 0.5 at.% of Ga however lay quite in the range of Xe-contents in this study and access to cryo-FIB equipment may nowadays be similarly as challenging as to a Xe<sup>+</sup>-pFIB. Either way, a lack of quantitative data from the modelling of local annealing effects by either Ga<sup>+</sup> or Xe<sup>+</sup> ion bombardment impedes the analysis of thermal effects upon bombardment. Nevertheless, the potential phase transformation due to the high diffusivity of Ga at Al interfaces clearly needs to be avoided to prevent false interpretation.

In conclusion, we report a phase transformation in an Al-Ni alloy caused by Ga<sup>+</sup> irradiation, and thus recommend Xe<sup>+</sup>-pFIB preparation instead to avoid sample modification by Ga. The evidence shows that conventional Ga<sup>+</sup>-FIB TEM sample preparation is able to induce phase transformations in nanocrystalline Al alloys. Thus, we expand the scope of observed phase transformation by Ga<sup>+</sup>-FIB bombardment beyond previously reported austenitic stainless steels [6,8–11]. This is a critical advancement that reveals previously unreported transformation in Al-alloys by Ga<sup>+</sup>-FIB, whereas transformation can be avoided in this case through Xe<sup>+</sup>-pFIB preparation. Ultimately, Ga<sup>+</sup>-FIB preparation may indeed affect a range of metastable solid solutions produced by magnetron sputtering, such as the FCC Al<sub>95</sub>Ni<sub>5</sub> here that has a low energy barrier for phase transformation.

#### CRedit authorship contribution statement

**Hendrik C. Jansen:** Writing – review & editing, Writing – original draft, Methodology, Investigation, Conceptualization. **Amit Sharma:** Writing – review & editing, Investigation. **Krzysztof Wiczerzak:**

Writing – review & editing, Investigation. **Ganesh K. Nayak:** Writing – review & editing, Investigation. **Jochen M. Schneider:** Writing – review & editing, Supervision, Funding acquisition. **Jakob Schwiedrzik:** Writing – review & editing, Supervision, Funding acquisition. **Thomas E.J. Edwards:** Writing – review & editing, Validation, Supervision, Methodology, Investigation, Conceptualization. **Johann Michler:** Writing – review & editing, Supervision, Resources, Funding acquisition, Conceptualization.

#### Declaration of competing interest

The authors declare that they have no known competing financial interests or personal relationships that could have appeared to influence the work reported in this paper.

#### Acknowledgements

H CJ was supported by the Innosuisse Innovation project 109.352.1 “ORALCOAT”. TEJE gratefully acknowledges the support of Innosuisse (42220.1 IP-ENG). K.W. was supported by the Polish National Agency for Academic Exchange under the Polish Returns Programme. GKN and JMS gratefully acknowledge the Ministry for Culture and Science of the State of North Rhine-Westphalia (MKW NRW) for supporting this work as part of the NHR funding. The authors gratefully acknowledge the computing time provided to them on the high-performance computer CLAIX at the NHR Center NHR4CES with project id p0020883. The authors gratefully acknowledge Dr. I. Utke, Dr. D. Casari, and ScopeM, particularly Dr. Joakim Reuteler, for their support & assistance in this work.

#### Supplementary materials

Supplementary material associated with this article can be found, in the online version, at [doi:10.1016/j.scriptamat.2025.116589](https://doi.org/10.1016/j.scriptamat.2025.116589).

#### References

- [1] L.A. Giannuzzi, F.A. Stevie, A review of focused ion beam milling techniques for TEM specimen preparation, *Micron* 30 (1999) 197–204.
- [2] L.A. Giannuzzi, F.A. Stevie, *Introduction to Focused Ion Beam Techniques: Instrumentation, Theory, Techniques and Practice*, Springer Science & Business Media, 2004.
- [3] J. Mayer, L.A. Giannuzzi, T. Kamino, J. Michael, TEM Sample Preparation and Damage, *MRS Bull* 32 (2007) 400–407.
- [4] B. Gault, A.J. Breen, Y. Chang, J. He, E.A. Jäggle, P. Kontis, P. Kürnsteiner, A. Kwiatkowski Da Silva, S.K. Makineni, I. Mouton, Z. Peng, D. Ponge, T. Schwarz, L.T. Stephenson, A. Szczepaniak, H. Zhao, D. Raabe, Interfaces and defect composition at the near-atomic scale through atom probe tomography investigations, *J. Mater. Res.* 33 (2018) 4018–4030.
- [5] X. Zhong, C.A. Wade, P.J. Withers, X. Zhou, C. Cai, S.J. Haigh, M.G. Burke, Comparing Xe<sup>+</sup>-pFIB and Ga<sup>+</sup>-FIB for TEM sample preparation of Al alloys: Minimising FIB-induced artefacts, *J. Microsc.* 282 (2021) 101–112.
- [6] J.R. Michael, L.A. Giannuzzi, M.G. Burke, X.L. Zhong, Mechanism of FIB-Induced Phase Transformation in Austenitic Steel, *Microsc. Microanal.* 28 (2022) 70–82.
- [7] L. Lilensten, B. Gault, New approach for FIB-preparation of atom probe specimens for aluminum alloys, *PLoS One* 15 (2020) 1–9.
- [8] K.E. Knippling, D.J. Rowenhorst, R.W. Fonda, G. Spanos, Effects of focused ion beam milling on austenite stability in ferrous alloys, *Mater. Charact.* 61 (2010) 1–6.
- [9] R.P. Babu, S. Irukuvarghula, A. Harte, M. Preuss, Nature of gallium focused ion beam induced phase transformation in 316L austenitic stainless steel, *Acta Mater.* 120 (2016) 391–402.
- [10] K. Shimizu, H. Tsuruta, Y. Kamada, T. Murakami, H. Watanabe, Crystallographic analysis of Ga<sup>+</sup> irradiation-induced phase transformation in austenitic stainless steels, *Mater. Charact.* 194 (2022) 112375.
- [11] A. Basa, C. Thaulow, A. Barnoush, Chemically induced phase transformation in Austenite by focused ion beam, *Metall. Mater. Trans. A Phys. Metall. Mater. Sci.* 45 (2014) 1189–1198.
- [12] J.F. Ziegler, M.D. Ziegler, J.P. Biersack, SRIM - The stopping and range of ions in matter, *Nucl. Instruments Methods Phys. Res. Sect. B Beam Interact. with Mater. Atoms* 268 (2010) 1818–1823, 2010.
- [13] K.A. Unocic, M.J. Mills, G.S. Daehn, Effect of gallium focused ion beam milling on preparation of aluminium thin foils, *J. Microsc.* 240 (2010) 227–238.
- [14] M.L. Taheri, J.T. Sebastian, B.W. Reed, D.N. Seidman, A.D. Rollett, Site-specific atomic scale analysis of solute segregation to a coincidence site lattice grain boundary, *Ultramicroscopy* 110 (2010) 278–284.

- [15] S. Ruan, K.L. Torres, G.B. Thompson, C.A. Schuh, Gallium-enhanced phase contrast in atom probe tomography of nanocrystalline and amorphous Al-Mn alloys, *Ultramicroscopy* 111 (2011) 1062–1072.
- [16] F. Tang, D.S. Gianola, M.P. Moody, K.J. Hemker, J.M. Cairney, Observations of grain boundary impurities in nanocrystalline Al and their influence on microstructural stability and mechanical behaviour, *Acta Mater.* 60 (2012) 1038–1047.
- [17] H. Zhao, F. De Geuser, A. Kwiatkowski da Silva, A. Szczepaniak, B. Gault, D. Ponge, D. Raabe, Segregation assisted grain boundary precipitation in a model Al-Zn-Mg-Cu alloy, *Acta Mater.* 156 (2018) 318–329.
- [18] A.W. Thompson, Z.D. Harris, J.T. Burns, Examination of focused ion beam-induced damage during platinum deposition in the near-surface region of an aerospace aluminum alloy, *Micron* 118 (2019) 43–49.
- [19] E. Pereiro-López, W. Ludwig, D. Bellet, Discontinuous penetration of liquid Ga into grain boundaries of Al polycrystals, *Acta Mater.* 52 (2004) 321–332.
- [20] B.A. Benson, R.G. Hoagland, Crack growth behavior of a high strength aluminum alloy during LME by gallium, *Scr. Metall.* 23 (1989) 1943–1948.
- [21] K. Thompson, D. Lawrence, D.J. Larson, J.D. Olson, T.F. Kelly, B. Gorman, In situ site-specific specimen preparation for atom probe tomography, *Ultramicroscopy* 107 (2007) 131–139.
- [22] Y. Yang, S.Y. Wang, B. Xiang, S. Yin, T.C. Pekin, X. Li, R. Zhang, K. Yano, D. Hwang, M. Asta, C. Grigoropoulos, F.I. Allen, A.M. Minor, Evaluating the effects of pillar shape and gallium ion beam damage on the mechanical properties of single crystal aluminum nanopillars, *J. Mater. Res.* 36 (2021) 2515–2528.
- [23] Y. Xiao, V. Maier-Kiener, J. Michler, R. Spolenak, J.M. Wheeler, Deformation behavior of aluminum pillars produced by Xe and Ga focused ion beams: Insights from strain rate jump tests, *Mater. Des.* 181 (2019) 107914.
- [24] N.L. Peterson, S.J. Rothman, Impurity Diffusion in Aluminum, *Phys. Rev. B.* 1 (1970) 10.
- [25] T. Xie, T.E.J. Edwards, N.M. della Ventura, D. Casari, E. Huszár, L. Fu, L. Zhou, X. Maeder, J.J. Schwiedrzik, I. Utke, J. Michler, L. Pethö, Synthesis of model Al-Al<sub>2</sub>O<sub>3</sub> multilayer systems with monolayer oxide thickness control by circumventing native oxidation, *Thin Solid Films* 711 (2020) 138287.
- [26] T.E.J. Edwards, T. Xie, N. Maria della Ventura, D. Casari, C. Guerra, E. Huszár, X. Maeder, J.J. Schwiedrzik, I. Utke, L. Pethö, J. Michler, On the thinnest Al<sub>2</sub>O<sub>3</sub> interlayers in Al-based nanolaminates to enhance strength, and the role of constraint, *Acta Mater.* 240 (2022) 118345.
- [27] B. Putz, T.E.J. Edwards, E. Huszar, P.A. Gruber, K.P. Gradwohl, P. Kreiml, D. M. Többsen, J. Michler, Electromechanical Behavior of Al/Al<sub>2</sub>O<sub>3</sub> Multilayers on Flexible Substrates: Insights from In Situ Film Stress and Resistance Measurements, *Adv. Eng. Mater.* 25 (2023).
- [28] B. Putz, T.E.J. Edwards, E. Huszar, L. Pethö, P. Kreiml, M.J. Cordill, D. Thiaudiere, S. Chiroli, F. Zighem, D. Faurie, P.O. Renault, J. Michler, In situ fragmentation of Al/Al<sub>2</sub>O<sub>3</sub> multilayers on flexible substrates in biaxial tension, *Mater. Des.* 232 (2023) 112081.
- [29] J.P. McCaffrey, M.W. Phaneuf, L.D. Madsen, Surface damage formation during ion-beam thinning of samples for transmission electron microscopy, *Ultramicroscopy* 87 (2001) 97–104.
- [30] M. Klinger, More features, more tools, more CrysTBox, *J. Appl. Crystallogr.* 50 (2017) 1226–1234.
- [31] J.R. Michael, Focused ion beam induced microstructural alterations: texture development, grain growth, and intermetallic formation, *Microsc. Microanal.* 17 (2011) 386–397.
- [32] A.J. Bradley, A. Taylor, XCIX. The crystal structures of Ni<sub>2</sub>Al<sub>3</sub> and NiAl<sub>3</sub>, *Dublin Philos. Mag. J. Sci.* 23 (1937) 1049–1067.
- [33] P. Kuisma-Kursula, Accuracy, Precision and Detection Limits of SEM-WDS, SEM-EDS and PIXE in the Multi-Elemental Analysis of Medieval Glass, *X-Ray Spectrom.* 29 (2000) 111–118.
- [34] M. Kim, J.M. Zuo, G.S. Park, High-resolution strain measurement in shallow trench isolation structures using dynamic electron diffraction, *Appl. Phys. Lett.* 84 (2004) 2181–2183.
- [35] V. Randle, I. Barker, B. Ralph, Measurement of lattice parameter and strain using convergent beam electron diffraction, *J. Electron Microsc. Tech.* 13 (1989) 51–65.
- [36] S. Fujinaka, Y. Sato, R. Teranishi, K. Kaneko, Understanding of scanning-system distortions of atomic-scale scanning transmission electron microscopy images for accurate lattice parameter measurements, *J. Mater. Sci.* 55 (2020) 8123–8133.
- [37] T. Shimizu, M. Zanaška, R.P. Vilhoan, N. Brenning, U. Helmersson, D. Lundin, Experimental verification of deposition rate increase, with maintained high ionized flux fraction, by shortening the HiPIMS pulse, *Plasma Sources Sci. Technol.* 30 (2021) 0–8.
- [38] G. Kresse, J. Furthmüller, Efficiency of ab-initio total energy calculations for metals and semiconductors using a plane-wave basis set, *Comput. Mater. Sci.* 6 (1996) 15–50.
- [39] J.P. Perdew, A. Zunger, Self-interaction correction to density-functional approximations for many-electron systems, *Phys. Rev. B.* 23 (1981) 5048–5079.
- [40] S.H. Wei, L.G. Ferreira, J.E. Bernard, A. Zunger, Electronic properties of random alloys: special quasirandom structures, *Phys. Rev. B.* 42 (1990) 9622–9649.
- [41] C. Michaelsen, G. Lucadamo, K. Barmak, The early stages of solid-state reactions in Ni/Al multilayer films, *J. Appl. Phys.* 80 (1996) 6689–6698.
- [42] K. Barmak, C. Michaelsen, G. Lucadamo, Reactive phase formation in sputter-deposited Ni/Al multilayer thin films, *J. Mater. Res.* 12 (1997) 133–146.
- [43] K. Larsen, N. Karpe, J. Bottiger, Ion irradiation induced phase formation in Al-Ni, *J. Mater. Res.* 7 (1992) 861–867.
- [44] J. Meingailis, Focused ion beam technology and ultimate applications, *J. Vac. Sci. Technol. B.* 5 (1987) 469–495.
- [45] T. Ishitani, H. Kaga, Calculation of local temperature rise in focused-ion-beam sample preparation, *J. Electron. Microsc. (Tokyo)*. 44 (1995) 331–336.
- [46] J.J. Jiménez, K. Jaekel, C. Pauly, C. Schäfer, H. Bartsch, F. Mücklich, F.M. Morales, Impact of sample preparation approach on transmission electron microscopy investigation of sputtered Al<sub>2</sub>Ni multilayers used for reactive soldering, *Adv. Eng. Mater.* 2302215 (2024) 1–12.